The Astrophysical Journal, 911:63 (12pp), 2021 April 10 https://doi.org/10.3847/1538-4357/abe9b4

Effects of Density Fluctuations on Alfvén Wave Turbulence in a Coronal Hole

M. Asgari-Targhi[1], A. Asgari-Targhi[1,2], M. Hahn[3], and D. W. Savin[3]
[1] Harvard-Smithsonian Center for Astrophysics, 60 Garden Street, Cambridge, MA 02138, USA
[2] Harvard Faculty of Arts and Sciences, Harvard University, Cambridge, MA 02138, USA
[3] Columbia Astrophysics Laboratory, Columbia University, 550 West 120th Street, New York, NY 10027, USA
Received 2020 September 24; revised 2021 February 18; accepted 2021 February 23; published 2021 April 16

Abstract

We present a study of density fluctuations in coronal holes. We used a reduced magnetohydrodynamic (RMHD) model that incorporated observationally constrained density fluctuations to determine whether density fluctuations in coronal holes can enhance Alfvén wave reflection and dissipation, thereby heating coronal holes and driving the fast solar wind. We show results for two models of the background atmosphere. Each model is a solution of the momentum equation and includes the effects of wave pressure on the solar wind outflow. In the first model, the plasma density and Alfvén speed vary smoothly with height. Wave reflection is relatively weak in the smooth model, resulting in a low energy dissipation rate. In the second model, we include additional density fluctuations along the flux tube based on the observations. We find that density ρ fluctuations on the order of $\delta\rho/\rho \sim 0.24$ increase the Alfvén wave turbulence to levels sufficient to heat the open field regions in coronal holes.

Unified Astronomy Thesaurus concepts: Solar physics (1476); The Sun (1693); Solar coronal heating (1989); Solar coronal holes (1484); Solar corona (1483); Solar atmosphere (1477)

1. Introduction

Coronal holes are regions of the solar atmosphere where the magnetic field is open and extends into interplanetary space. Their temperatures and densities are lower than the surrounding closed field regions, known as the quiet Sun, and are the primary source of the fast solar wind, with velocities in the range of 500–800 km s^{-1} (Munro & Withbroe 1972; Krieger et al. 1973; Zirker 1977). Many physical mechanisms have been proposed to explain the energization and the acceleration of plasma emanating from coronal holes and the ensuing fast solar wind. Alfvén waves, which are ubiquitous in the corona (De Pontieu et al. 2007; Tomczyk et al. 2007; Tomczyk & McIntosh 2009; Hahn & Savin 2013; Tian et al. 2014; Morton et al. 2015), are one such mechanism; and Alfvén wave turbulence is one of the major theories considered to explain the heating of coronal holes (Parker 1965; Heinemann & Olbert 1980; Velli 1993; Suzuki & Inutsuka 2006; Cranmer et al. 2007; Hollweg & Isenberg 2007).

In coronal holes, Alfvén waves are believed to be generated at the photosphere by the underlying granular convective flows that interact with open magnetic field lines, launching waves that travel along the field lines in the corona (Parker 1965; Dmitruk et al. 2002; Verdini et al. 2009; Cranmer et al. 2015). The waves are reflected in the corona by the radial gradients in the Alfvén speed, producing inward propagating waves (Heinemann & Olbert 1980; Velli 1993). These inward propagating waves interact nonlinearly with the outward propagating waves, driving turbulence, and generate heating (Zhou & Matthaeus 1990; Matthaeus et al. 1999; Chandran et al. 2009).

Observational studies of Alfvén waves indicate that the waves carry and deposit enough energy at sufficiently low heights to explain the heating of coronal holes (Bemporad & Abbo 2012; Hahn et al. 2012; Hahn & Savin 2013; Hara 2019). However, models that assume that the magnetic field and particle density decrease smoothly with height predict insufficient reflection of the Alfvén waves and correspondingly insufficient generation of the turbulence needed to match the energy loss inferred from the observations. A potential solution would be if there were density fluctuations along the open field lines. Our models indicate that these density fluctuations increase the rate of Alfvén wave reflection and dissipation, creating more turbulence, and thereby increasing the heating rate (van Ballegooijen & Asgari-Targhi 2016, 2017).

There is strong observational evidence for density fluctuations in coronal holes (Banerjee et al. 2011; Miyamoto et al. 2014; Hahn et al. 2018). In this paper, we use these observations to constrain a three-dimensional (3D) RMHD turbulence model. Incorporating these density fluctuations into our model, we find that the observed density fluctuations increase wave reflection and turbulent dissipation to levels sufficient to heat the open field regions in coronal holes.

The rest of this paper is organized as follows. Section 2 describes the density fluctuation observations. In Section 3, we present our 3D RMHD model of Alfvén wave turbulence in a coronal hole. Some of the details, including the derivations of the equations, are presented in the Appendix. The simulation results for a smooth model are shown in Section 4, where the turbulence dissipation rates are compared with those needed to maintain and energize the background atmosphere. Section 5 implements the observed density fluctuations from Section 2 and considers their effects on the turbulence and the heating rates. Section 6 discusses the significance of our results in understanding the energization and acceleration of the fast solar wind.

2. Density Fluctuation Observations in Coronal Holes

Density fluctuation observations from Hahn et al. (2018) are shown in Figure 1(a) as a function of height in a polar coronal hole up to a radius of $\approx 1.3\ R_\odot$. These fluctuations were inferred from a series of images of the Sun in the 174 Å bandpass using the Sun Watcher using Active Pixel System (SWAP; Halain et al. 2013; Seaton et al. 2013), instrument on the Project for Onboard Autonomy (Proba2, Santandrea et al. 2013) satellite. The coronal density fluctuation amplitudes were inferred by obtaining the total rms intensity fluctuation amplitude at each

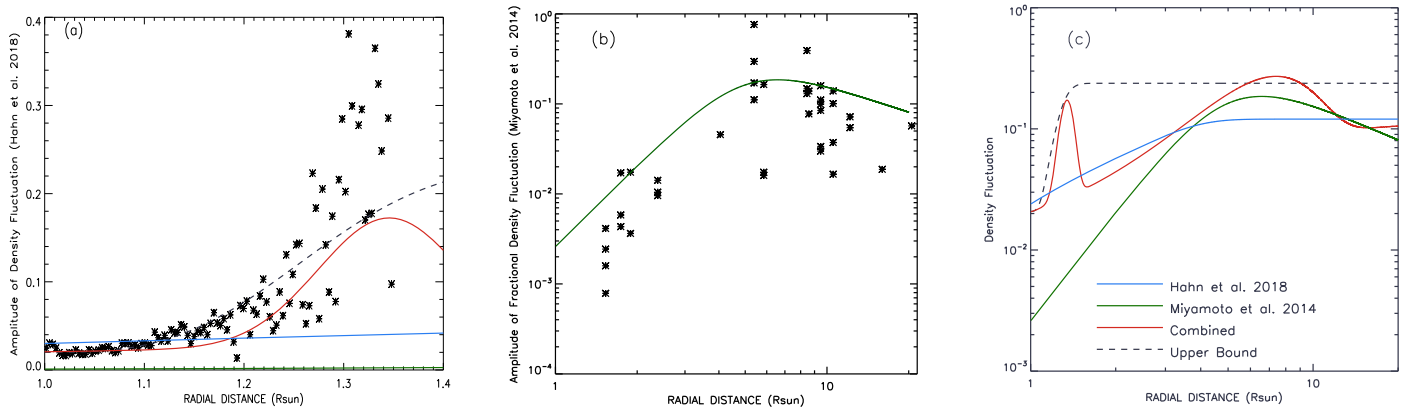

Figure 1. (a) Estimates of density fluctuations as a function of position between 1.00 and 1.35 $R_\odot$ in a coronal hole based on observations from Hahn et al. (2018; black stars). The blue curve is an estimated lower bound to the data points, the dashed black curve is an estimated upper bound, and the red curve is explained in (c). (b) Amplitude of density fluctuations from 1.5 to 20.5 $R_\odot$ from the observations by Miyamoto et al. (2014; black stars) , which we incorporate into our model using the green curve. (c) Extrapolations in the limit of 1–20 $R_\odot$, from Hahn et al. (2018; blue curve), from Miyamoto et al. (2014; green curve), the two observations combined (red curve), and the upper bound to Hahn et al. (2018) and Miyamoto et al. (2014) observations (dashed black curve). See the text for details.

pixel, and subtracting from that estimates for the photon and detector noise. In estimating the rms fluctuation, it is necessary to define an average value about which the fluctuations occur. Here, we use the data of Hahn et al. (2018) calculated using a running-difference method that measured fluctuations relative to the average over a 20 minute window. The average SWAP intensity is also uncertain due to instrument scattered light, which influences the normalization of the density fluctuations. Here, we have used the normalization based on the observed scattered light during a solar eclipse. Additional details about the plotted data can be found in Hahn et al. (2018). For clarity, we have omitted the statistical uncertainties in Figure 1(a).

Observations of density fluctuations at larger heights have been obtained by Miyamoto et al. (2014). They used the Akatsuki spacecraft radio occultation technique to infer density fluctuations at heights of 1.5–20.5 $R_\odot$. As the spacecraft passed behind the Sun, from 2011 June 6 to July 8, it emitted radio waves that were detected at the Earth. Density fluctuations in the corona caused frequency fluctuations in the detected signal. Miyamoto et al. (2014) estimated the amplitude of the density fluctuations using these frequency fluctuations. Their results are illustrated in Figure 1(b). There are a number of possible sources of systematic uncertainty in these results. Using a different estimate of the average coronal density would change their results by a factor of 2–3. Their analysis assumes that the density fluctuations are outward propagating acoustic waves; but if the waves were inward propagating, then the fluctuations would be larger by a factor of 2–30. In addition, the consideration of single wavelength fluctuations, the limited frequency range measured, and the selection of statistically significant peaks in the observations make it likely that the inferred fluctuations are underestimated.

The density fluctuations presented here have been attributed to compressive waves in solar wind (Kudoh & Shibata 1999; Moriyasu et al. 2004; Matsumoto & Shibata 2010). The Hahn et al. (2018) and Miyamoto et al. (2014) observations find that the density fluctuation amplitude increases with height in the corona out to several solar radii, but there appears to be a difference in the magnitude of these fluctuations. Although, the data sets do not overlap in height, the Hahn et al. (2018) measurements appear to be systematically larger than those of Miyamoto et al. (2014). Several factors may contribute to this disparity. First, different solar structures were present in the observations. Hahn et al. (2018) observed a coronal hole observed near solar minimum, whereas Miyamoto et al. (2014) observed the Sun during the rising phase of a solar cycle when no major coronal holes were present. Second, as mentioned above, there are several assumptions in the Miyamoto et al. (2014) analysis that would tend to produce an underestimate of the fluctuation amplitude. Finally, there are significant statistical uncertainties in the Hahn et al. (2018) data at their largest heights, which may reduce some of the apparent disparity.

We have used these empirical measurements as the basis for the density fluctuation amplitude input into our model, which extends from the base of the corona at $1\,R_\odot$ up to $20\,R_\odot$. For this, we have combined the observations by Hahn et al. (2018) and Miyamoto et al. (2014). We have obtained plausible curves to connect these measurements and assess the uncertainties based on the upper and lower bounds. All of these curves are shown in Figure 1(c). The blue curve is an estimated lower bound to the data of Hahn et al. (2018) and extrapolates to heights above $1.35\,R_\odot$ to approximately match the results of Miyamoto et al. (2014) at $20\,R_\odot$. The green curve represents the Miyamoto et al. (2014) observation and extrapolates the data down to $1\,R_\odot$. The dashed black curve is an estimated upper bound to the observations of Hahn et al. (2018) and Miyamoto et al. (2014). The red curve is an approximation between the two data sets that falls in between the observations by Hahn et al. (2018) and Miyamoto et al. (2014) at low heights.

3. Alfvén Wave Turbulence Model of a Coronal Hole

Alfvén waves are transverse incompressible magnetic oscillations (Alfvén 1947) and are ubiquitous in the solar atmosphere (De Pontieu et al. 2007; Tomczyk et al. 2007; Tomczyk & McIntosh 2009; Morton et al. 2015). We describe the nonlinear dynamics of Alfvén waves in a thin flux tube inside a coronal hole using the RMHD equations. The flux tube is positioned at the coronal base, $r_{\rm base} = 1.003\,R_\odot$, and expands radially outward to $r = 20\,R_\odot$. The flux tube is assumed to have a square cross section with size $2R(r)$ and refer to $R(r)$ as the flux tube radius. We described the details of this model in van Ballegooijen & Asgari-Targhi (2016, 2017). The Alfvén waves are launched at the coronal base by introducing

incompressible footpoint motions. The footpoint motions are restricted to the square cross section and have a velocity amplitude $v_{\rm rms} \approx 40\ {\rm km\ s^{-1}}$. This velocity is in agreement with the spectral line widths and nonthermal velocities observed at the base of coronal holes (Wilhelm et al. 1998; McIntosh et al. 2008; Banerjee et al. 2009; Landi & Cranmer 2009; Singh et al. 2011; Bemporad & Abbo 2012; Hahn et al. 2012). The footpoint motions have a correlation length $\lambda_\perp = 1$ Mm, where $\lambda_\perp(r)$ is the perpendicular correlation length of the turbulence. In the present work we use a correlation time $\tau_{\rm c} \approx 48$ s. We adopted this value so that the correlation time is comparable to the timescale of the solar granulation.

In the present model, the background atmosphere is highly inhomogeneous, the outward propagating waves are launched at the coronal base, and the inward propagating waves are produced by wave reflections. We define the Alfvén waves in terms of their effect on magnetic field $B(r, t)$ and plasma velocity $v(r, t)$, both functions of position r within the flux tube and time t. The plasma motions are expressed by the MHD equations in 3D:

$$\frac{\partial \rho}{\partial t} + \nabla \cdot (\rho \boldsymbol{v}) = 0, \tag{1}$$

$$\rho \frac{d\boldsymbol{v}}{dt} = -\nabla p + \frac{1}{4\pi}(\nabla \times \boldsymbol{B}) \times \boldsymbol{B} - \rho \frac{GM_\odot}{r^2}\hat{\boldsymbol{r}} + \boldsymbol{D}_{\rm v}, \tag{2}$$

$$\rho\left[\frac{d}{dt}\left(\frac{1}{\gamma - 1}\frac{p}{\rho}\right) + p\frac{d}{dt}\left(\frac{1}{\rho}\right)\right] = Q_{\rm A} - Q_{\rm rad} - Q_{\rm cond}, \tag{3}$$

$$\frac{\partial \boldsymbol{B}}{\partial t} = \nabla \times (\boldsymbol{v} \times \boldsymbol{B}) + \boldsymbol{D}_{\rm m}, \tag{4}$$

where r denotes the position, and t is time, $\rho(r, t)$ is the mass density, $p(\boldsymbol{r}, t)$ is the plasma pressure, $\boldsymbol{B}$ is the magnetic field strength, G is the gravitational constant, $M_\odot$ is the solar mass, $\hat{\boldsymbol{r}}$ is the unit vector in the radial direction, and $\boldsymbol{D}_{\rm v}$ and $\boldsymbol{D}_{\rm m}$ are dissipative terms. In the heat Equation (3), γ is the ratio of specific heat coefficients, $Q_{\rm A}(r, t)$ is the plasma heating rate per unit volume and includes the viscous term and the Joule heating term, $Q_{\rm rad}(r, t)$ is the radiative loss rate, and $Q_{\rm cond}(r, t)$ is the conductive loss rate. $Q_{\rm cond}$ is given by the divergence of the conductive flux, $Q_{\rm cond} = \nabla \cdot \boldsymbol{F}_{\rm cond}$, which may be positive or negative depending on position in the corona. The conductivity tensor is highly anisotropic and the resulting conductive flux $\boldsymbol{F}_{\rm cond}$ is nearly parallel to the magnetic field $\boldsymbol{B}$.

We first set up a background atmosphere for wave propagation in the expanding flux tube using the model developed in van Ballegooijen & Asgari-Targhi (2016, 2017). The parameters used in the set up of the background atmosphere are introduced with the subscript 0. In addition to the magnetic field strength $B_0(r)$, we also need the plasma temperature $T_0(r)$, density $\rho_0(r)$, and outflow velocity $u_0(r)$. The Appendix describes how these quantities are computed. In our modeling, there is a distinction between the total wave energy dissipation rate $Q_{\rm tot}$ and the plasma heating rate $Q_{\rm A}$. The term $Q_{\rm tot}$ is updated by solving the RMHD equations at each time step while $Q_{\rm A}$ is calculated from the background atmosphere model and does not change. If the waves provide all the heating, these two rates should be equal, $Q_{\rm tot} = Q_{\rm A}$. The objective of the present work is to construct a solar wind model for which this condition is satisfied.

Figure 2 shows the radial profile of some of the background parameters. Figure 2(a) shows the density. The density $\rho_0(r)$ and outflow velocity $u_0(r)$ are computed from iteratively solving the mass flux conservation, momentum, and energy equations. Figure 2(b) shows the temperature $T_0(r)$ computed from Equations (A16)–(A18). Figure 2(c) shows the magnetic field strength $B_0(r)$ as determined from Equation (A15) with $B_{\rm pole} = 10$ G.

Figure 2(d) shows the outflow velocity $u_0(r)$ of the solar wind, the sound speed $c_{\rm s}$, and the Alfvén speed $v_{\rm A}$. The critical point of the outflow or the sonic point is at $r_{\rm c} \approx 1.8\ R_\odot$ with the velocity $c_{\rm s} \approx 168\ {\rm km\ s^{-1}}$. Above this velocity the solar wind is supersonic. When the wave pressure force $D_{\rm wp}$ given by Equation (A4) is absent, the sonic point is at $r \approx 4.48\ R_\odot$. Therefore, the wave pressure force plays a dominant role in creating and energizing the fast solar wind (Belcher 1971; Hollweg 1973; Jacques 1978). The Alfvén critical point, where the two curves $u_0(r)$ and $v_{\rm A}(r)$ cross each other is at $r \approx 7.2\ R_\odot$, and the velocity at this point is $624\ {\rm km\ s^{-1}}$. The Alfvén speed reaches a maximum of $v_{\rm A} \approx 2175\ {\rm km\ s^{-1}}$ at $r \approx 1.3\ R_\odot$.

Figure 2(e) displays the absolute value of the acceleration of gravity, and the acceleration $D_{\rm wp}/\rho_0$ produced as a result of wave pressure force. The wave pressure acceleration overtakes the gravitational acceleration at the height $r \approx 2\ R_\odot$. Figure 2(f) shows the total plasma heating rate $Q_{\rm A}(r)$ with contributions from radiative losses $Q_{\rm rad}(r)$ (blue curve), thermal conduction $Q_{\rm cond}(r)$, and advection $Q_{\rm adv}(r)$ given by Equation (A9).

3.1. RMHD Turbulence

Using the background atmosphere presented in the Appendix, we simulate the wave propagation in 3D using the time-dependent RMHD approximation. The waves are described in terms of the Elsässer variables:

$$\boldsymbol{z}_\pm \equiv \boldsymbol{v}_1 \mp \boldsymbol{B}_1/\sqrt{4\pi\rho_0}, \tag{5}$$

where $\boldsymbol{B}_1(\boldsymbol{r}, t)$ and $\boldsymbol{v}_1(\boldsymbol{r}, t)$ are the magnetic and velocity perturbations of the waves, and $\rho_0(r)$ is the plasma density. The term z_+ describes waves propagating outward and are referred to as "outward" waves. The term z_- describes the "inward" waves. In an inhomogeneous atmosphere, such as the solar wind, where the Alfvén speed varies strongly with position r, the inward waves can have both inward and outward propagating components (Velli et al. 1989; Perez & Chandran 2013). The RMHD equations are written in terms of the Elsässer variables, $\omega_\pm$, and they take the form

$$\frac{\partial \omega_\pm}{\partial t} = -(u_0 \pm v_{\rm A})\frac{\partial \omega_\pm}{\partial r} + \frac{1}{2} \times \left(\frac{dv_{\rm A}}{dr} \pm \frac{u_0}{2H_\rho}\right)(\omega_+ - \omega_-) + \frac{u_0}{2H_{\rm B}}(\omega_+ + \omega_-) - \frac{1}{2}[\omega_+, f_-] - \frac{1}{2}[\omega_-, f_+] \pm \nabla_\perp^2\left(\frac{1}{2}[f_+, f_-]\right), \tag{6}$$

where $f_\pm(\boldsymbol{r}, t)$ are the velocity stream functions of the Elsässer variables, $\omega_\pm \equiv -\nabla_\perp^2 f_\pm$ are the vorticities, $H_{\rm B}(r) \equiv B_0/(dB_0/dr)$ is the magnetic scale length, and $H_\rho(r) \equiv \rho_0/(d\rho_0/dr)$ is the density scale length. Note that u_0 and the radial gradients of B_0 and ρ_0 cause linear coupling between the ω_+ and ω_- waves. The first term on the right-hand side of this

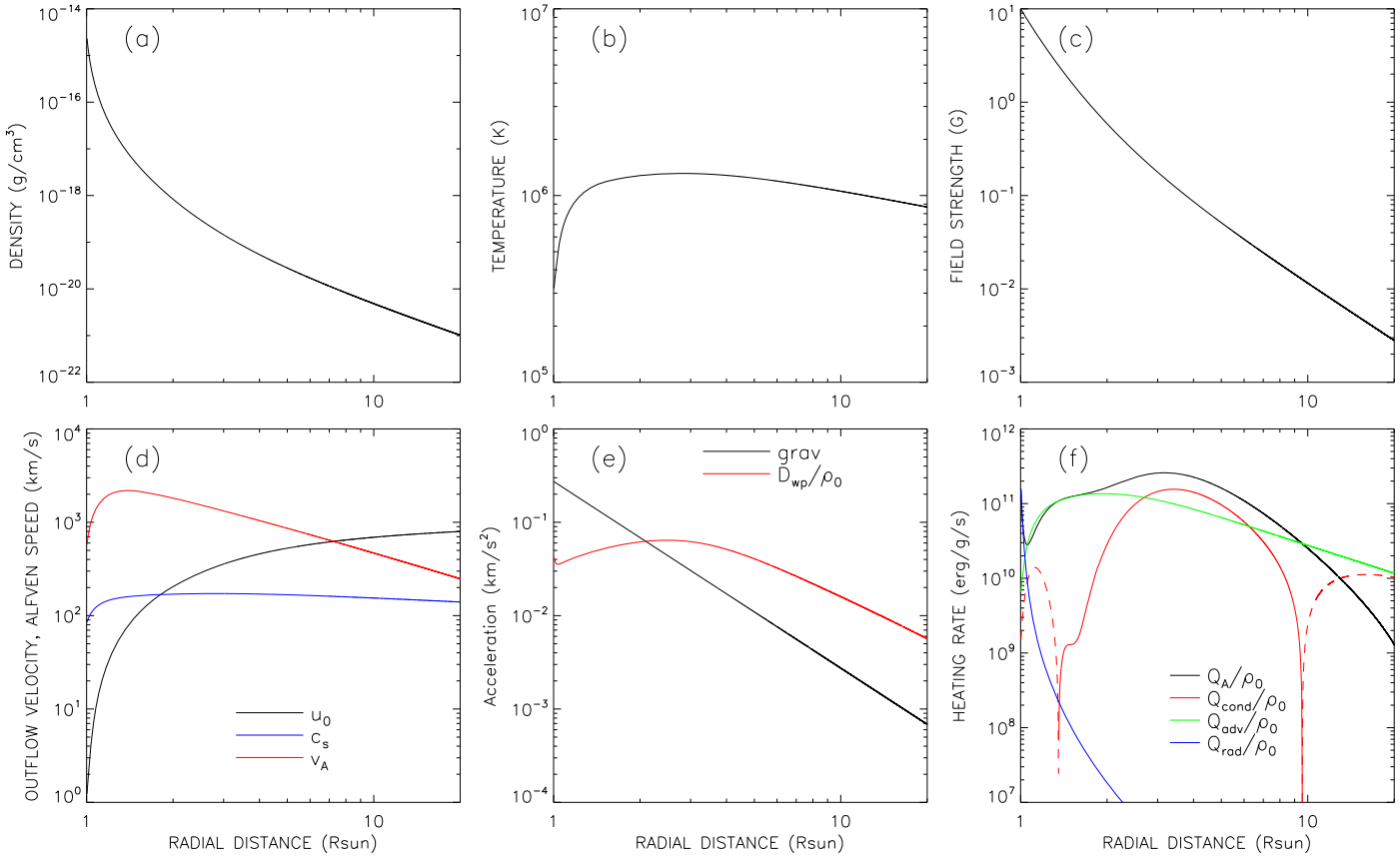

Figure 2. Radial dependence of various background quantities for a polar coronal hole. (a) Mass density. (b) Temperature. (c) Magnetic field strength. (d) Outflow velocity, u_0 (black curve), sound speed, c_s (blue curve), and Alfvén speed, v_A (red curve). (e) Absolute value of the inward acceleration due to gravity (black curve), and outward acceleration due to wave pressure gradient (red curve). (f) Plasma heating rate per unit mass due to wave dissipation (black curve), and energy loss rates per unit mass due to thermal conduction (red curve), advection (green curve), and radiation (blue curve). The red dashed curves indicate the region where the thermal conduction heats the plasma by conduction from below.

equation describes the effects of wave propagation, and the second and third terms describe the linear couplings between the outward and inward waves, respectively. The bracket operator $[\cdots, \cdots]$ is defined by

$$b(x, y, r, t) = [f, g] \equiv \frac{\partial f}{\partial x}\frac{\partial g}{\partial y} - \frac{\partial f}{\partial y}\frac{\partial g}{\partial x}, \tag{7}$$

where x and y are the coordinates perpendicular to the flux tube axis, and $f(x, y, r, t)$ and $g(x, y, r, t)$ are two arbitrary functions. All nonlinearities of the RMHD model are contained within such bracket terms. In Equation (6) we omit the dissipative terms, which will be described in more detail below.

Most RMHD models use a spectral method in which all functions of x and y are written in terms of a set of normalized basis functions $\tilde{F}_k(\tilde{x}, \tilde{y})$. Here $\tilde{x}$ and $\tilde{y}$ are dimensionless coordinates, and index k is in the range $k = 1, \cdots, k_{\max}$, where $k_{\max}$ is the total number of modes. Then an arbitrary function $f(x, y, r, t)$ can be written as

$$f(x, y, r, t) = \sum_k f_k(r, t)\tilde{F}_k(\tilde{x}, \tilde{y}), \tag{8}$$

where $f_k(r, t)$ is the amplitude of the mode with index k. The basis functions depend on the dimensionless perpendicular coordinates $\tilde{x} \equiv x/R(r)$ and $\tilde{y} \equiv y/R(r)$, where $R(r)$ is the radius of the cross section of the flux tube. We assume a square cross section, $-1 \leqslant \tilde{x} \leqslant +1$ and $-1 \leqslant \tilde{y} \leqslant +1$, and we use periodic boundary conditions on this square domain. Then the basis functions are products of $\tilde{x}$- and $\tilde{y}$-dependent parts, each of which are sine or cosine functions with periods $\Delta\tilde{x} = \Delta\tilde{y} = 2$. In this case Equation (8) is essentially the Fourier Transform written in a compact form. The width of the computational domain in dimensional units is $\Delta x = \Delta y = 2R(r)$, which increases with radial distance r from Sun center. The basis functions have well-defined dimensionless perpendicular wavenumbers $_{ax,k} = \pi\, n_{x,k}$ and $a_{y,k} = \pi\, n_{y,k}$, where $n_{x,k}$ and $n_{y,k}$ are integers. The total dimensionless wavenumber is $a_k \equiv \sqrt{a_{x,k}^2 + a_{y,k}^2}$, and the actual wavenumber in physical units is $k_\perp = a_k/R(r)$. Inserting Equation (8) into Equation (7), we find for the mode amplitudes of the function $b(x, y, r, t)$:

$$b_k(r, t) = \frac{1}{R^2(r)}\sum_j\sum_i M_{kji} f_j(r, t) g_i(r, t), \tag{9}$$

where $f_j(r, t)$ and $g_i(r, t)$ are the mode amplitudes of the arbitrary functions $f(x, y, r, t)$ and $g(x, y, r, t)$, and M_{kji} is a sparse, dimensionless matrix describing the nonlinear coupling between certain mode triples (i, j, k). For the present case of a

square cross section:

$$M_{kji} = \frac{1}{4}\int_{-1}^{+1}\int_{-1}^{+1} \tilde{F}_k(\tilde{x},\,\tilde{y}) \times \left(\frac{\partial \tilde{F}_j}{\partial \tilde{x}}\frac{\partial \tilde{F}_i}{\partial \tilde{y}} - \frac{\partial \tilde{F}_j}{\partial \tilde{y}}\frac{\partial \tilde{F}_i}{\partial \tilde{x}}\right) d\tilde{x}\; d\tilde{y}. \quad (10)$$

In general the details of the M_{kji} matrix depend on whether the flux tube has a circular or square cross section, and on the type of boundary condition used, but the matrix is always fully antisymmetric in its indices, as was shown for the circular case in Appendix B of van Ballegooijen et al. (2011). Using Equation (8), the RMHD equations can be written as

$$\frac{\partial \omega_{\pm,k}}{\partial t} = -(u_0 \pm v_{\rm A})\frac{\partial \omega_{\pm,k}}{\partial r} + \frac{1}{2}\left(\frac{dv_{\rm A}}{dr} \pm \frac{u_0}{2H_\rho}\right)(\omega_{+,k} - \omega_{-,k}) + \frac{u_0}{2H_{\rm B}}(\omega_{+,k} + \omega_{-,k}) + \frac{1}{2R^4}\sum_j\sum_i M_{kji}(a_i^2 - a_j^2 - a_k^2) f_{\pm,j} f_{\mp,i} - \nu_{\pm,k}\,\omega_{\pm,k}, \quad (11)$$

where $\nu_{\pm,k}$ are artificial damping rates for outward and inward waves. The damping model is described in more detail in Section 3 of van Ballegooijen & Asgari-Targhi (2017).

Multiplying Equation (11) by $\frac{1}{2}\rho_0 f_{\pm,k}$ and summing over modes, we obtain the wave energy equations for the outward and inward waves:

$$\frac{\partial U_\pm}{\partial t} + B_0\frac{\partial}{\partial r}\left(\frac{F_\pm}{B_0}\right) = -u_0 D_\pm \mp \frac{1}{2}\frac{dv_{\rm A}}{dr}U_{\rm R} - Q_\pm, \quad (12)$$

where

$$U_\pm = \frac{\rho_0}{4R^2}\sum_k a_k^2 f_{\pm,k}^2, \quad (13)$$

$$U_{\rm R} = \frac{\rho_0}{2R^2}\sum_k a_k^2 f_{+,k} f_{-,k}, \quad (14)$$

$$Q_\pm = \frac{\rho_0}{2R^2}\sum_k \nu_{\pm,k} a_k^2 f_{\pm,k}^2, \quad (15)$$

$$F_\pm = (u_0 \pm v_{\rm A})U_\pm + \frac{1}{2}u_0\left(U_\pm - \frac{U_{\rm R}}{2}\right), \quad (16)$$

$$D_\pm = -\frac{1}{2}\frac{\partial}{\partial r}\left(U_\pm - \frac{U_{\rm R}}{2}\right) - \frac{U_{\rm R}}{2H_{\rm B}}, \quad (17)$$

and we use mass conservation ($\rho_0\; u_0/B_0 = $ constant). Here $U_\pm(r,\,t)$ are the wave energy densities, $U_{\rm R}\,(r,\,t)$ is the "residual" energy density (Grappin et al. 1982, 1983), $Q_\pm(r,\,t)$ are the wave dissipation rates, $F_\pm(r,\,t)$ are the energy fluxes, and $D_\pm(r,\,t)$ are the contributions to the wave pressure force. The total wave energy density is given by $U_{\rm tot} = U_+ + U_-$, and the contributions from magnetic and kinetic energy are given by $U_{\rm mag} = (U_{\rm tot} - U_{\rm R})/2$ and $U_{\rm kin} = (U_{\rm tot} + U_{\rm R})/2$. Similarly, the total dissipation rate $Q_{\rm tot} = Q_+ + Q_-$, the total energy flux $F_{\rm tot} = F_+ + F_-$, and the total wave pressure force $D_{\rm wp} = D_+ + D_-$. Note that the nonlinear terms in the RMHD equations drop out in the energy Equations (12) (also see Appendix C of van Ballegooijen & Asgari-Targhi 2016). The terms $u_0 D_\pm$ in the energy equations represent the work done by the wave pressure forces on the background flow.

4. Turbulence in a Model with a Smooth Background Atmosphere

The atmospheric model shown in Figure 2 is used as a background for the 3D, time-dependent simulations of Alfvén waves inside a thin flux tube described by Equation (6). The waves are launched at the coronal base, and they produce reflection driven turbulence at larger heights. We simulate the waves for 30,000 s. The waves reach the outer boundary at $r = 20\; R_\odot$ at 10,859 s.

Figure 3 shows the wave-related parameters averaged over the cross section of the flux tube and over time. The time interval is $t_0(r) + 300 \leqslant t \leqslant 30000$ (in seconds), where $t_0(r)$ is the time when an outward propagating wave reaches a certain height r. Figure 3(a) shows that the rms velocity amplitude of the waves, $v_{\rm rms}$, reaches a maximum of 292 km s^{-1} at $r \approx 5\; R_\odot$. Figure 3(a) also shows the rms values of the Elsässer variables, $Z_\pm(r) = \sqrt{\langle |z_\pm|^2 \rangle}$. The inward waves, $Z_-(r)$ are much weaker than outward waves, $Z_+(r)$. The amplitude of the inward waves has a sharp minimum at 1.3 $R_\odot$, presumably because the Alfvén speed has a maximum near this height.

Figure 3(b) presents the total energy density $U_{\rm tot}$ of the simulated waves, with contributions from the kinetic energy $U_{\rm kin}$ and magnetic energy density $U_{\rm mag}$. The dashed curve shows the energy density $U_{\rm A}$ used in the setup of the background atmosphere. The figure shows that $U_{\rm kin} \approx U_{\rm mag}$ and $U_{\rm tot} \approx U_{\rm A}$. Therefore, the wave simulation results are consistent with the assumptions made in the model setup of the background atmosphere (see the Appendix).

Figure 3(c) shows the total energy dissipation rate $Q_{\rm tot}(r)$ of the simulated turbulence, and the plasma heating rate $Q_{\rm A}(r)$ used in the setup of the background atmosphere. Note that the dissipation rate, $Q_{\rm tot}(r)$ is smaller than the plasma heating $Q_{\rm A}(r)$ over a wide range of heights in the smooth model. Therefore, in the smooth model presented here the simulated wave turbulence does not generate enough heating to raise the temperature to the assumed level $T_0(r)$ shown in Figure 2(b).

Figure 3(d) shows the same heating rates per unit mass. The total heating rate $Q_{\rm tot}(r)/\rho_0$ drops at 1.3 $R_\odot$, near the position where the Alfvén speed reaches its maximum, and the amplitude of the inward waves decreases. Figure 3(d) illustrates that the heating rate $Q_{\rm tot}\;(r)/\rho_0$ in the smooth model is insufficient to maintain the temperature of the background atmosphere needed to energize and accelerate the fast solar wind.

5. Turbulence in a Model with Density Fluctuations

We showed in Section 4, that in a solar wind model with a smooth background atmosphere, the energy dissipation rate $Q_{\rm tot}(r)$ produced from the Alfvén wave turbulence is much less than the energy $Q_{\rm A}(r)$ needed to heat the plasma and accelerate the solar wind. Therefore, the smooth model is inconsistent from the energy point of view. A mechanism is needed that increases the heating rate $Q_{\rm tot}$ without changing $Q_{\rm A}$. In the Alfvén wave turbulence model, turbulence is generated as a result of nonlinear interactions between counter-propagating waves. One means to increase the wave dissipation rate would

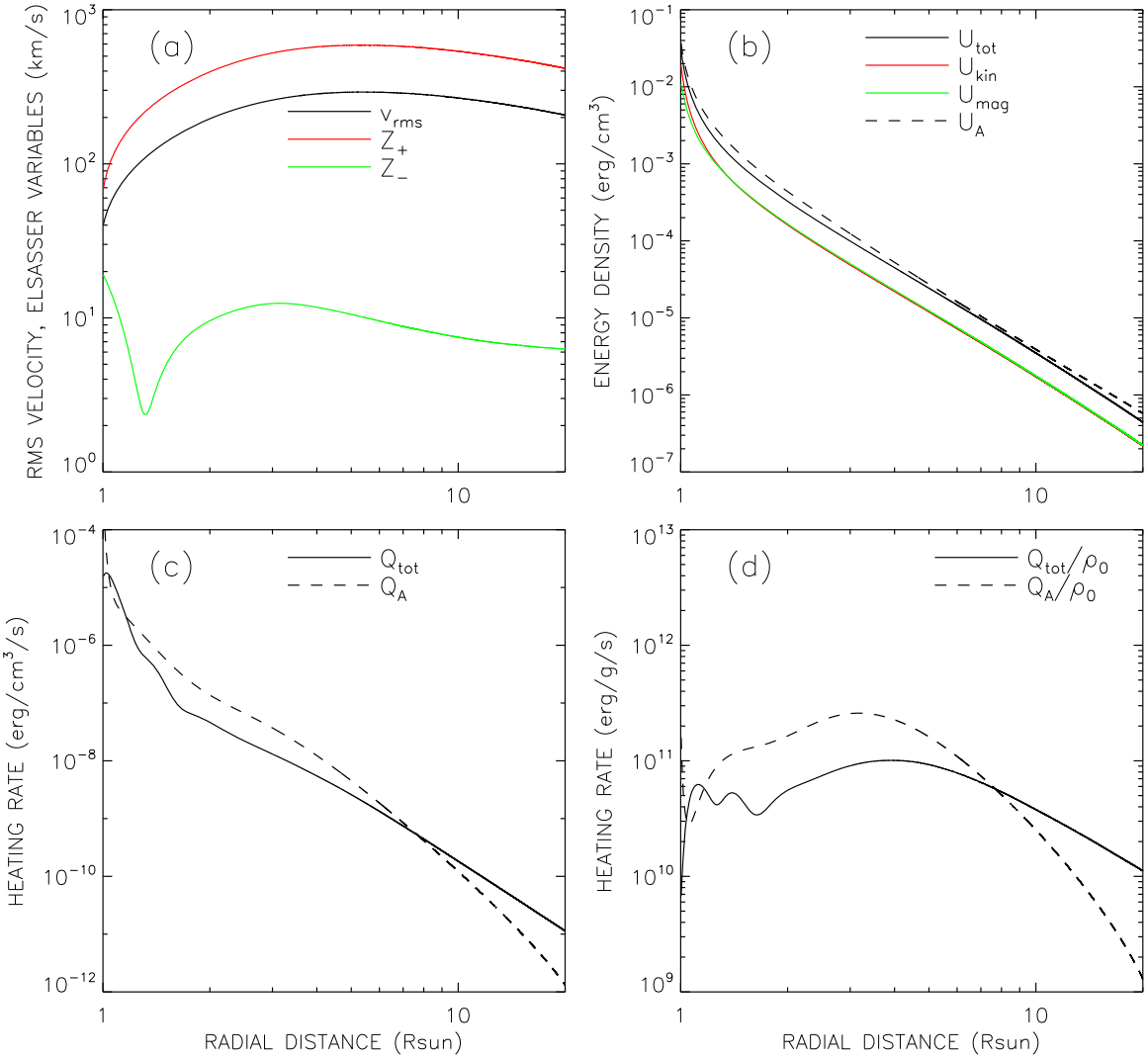

Figure 3. Radial dependence of wave-related quantities for a polar coronal hole model with a smooth background atmosphere. (a) Velocity amplitude of the waves (v_{rms}, black curve), and the rms values for the Elsässer variables for outward waves (Z_+, red curve) and inward waves (Z_-, green curve). (b) Wave energy densities: total energy (U_{tot}, black curve), kinetic energy (U_{kin}, red curve), magnetic energy (U_{mag}, green curve), and the wave energy density assumed in the set up of the background atmosphere (U_A, dashed black curve). (c) Wave energy dissipation rates per unit volume: total energy dissipation rate (i.e., heating rate) of the simulated turbulence (Q_{tot}, solid black curve), and plasma heating rate (Q_A, dashed black curve), assumed in the setup of the background atmosphere (dashed black curve). (d) Wave energy dissipation rates per unit mass: the rate derived from the turbulence simulation (Q_{tot}/ρ_0, solid black curve), and the rate assumed in the setup of the background atmosphere (Q_A/ρ_0, dashed curve).

be the creation of more wave reflection, which would enhance the intermixing of the waves and increase the turbulence. We can achieve this by introducing density fluctuations $\delta\rho(r, t)$. The observational evidence for density fluctuation was discussed in Section 2.

In this section, we consider a series of models that includes the effects of density fluctuations on the Alfvén waves. We include the density variations in our prescribed background atmosphere. The density fluctuations are considered to be random in position and stationary, i.e., independent of time. We first set up a model with spatial variations in density $\delta\rho(r)$. This is obtained by taking the solution from the "smooth model" described in Sections 3 and 4, and adding variations to some of the physical parameters. The density is determined from

$$\rho_0'(r) = \rho_0(r)[1 + \epsilon(r)], \tag{18}$$

where ρ_0 (r) is the density in the smooth model and $\epsilon(r) \equiv \delta\rho/\rho_0$ is a random function of position and is defined below. The Alfvén speed is

$$v_A'(r) = v_A(r)[1 + \epsilon(r)]^{-1/2}, \tag{19}$$

where $v_A(r)$ is the Alfvén speed in the smooth model. To conserve mass and preserve the same mass flux as in the smooth model, we consider the outflow velocity to be

$$u_0'(r) = u_0(r)/[1 + \epsilon(r)], \tag{20}$$

where $u_0(r)$ is the outflow velocity in the smooth model. We assume that the temperature $T_0(r)$ and magnetic field strength $B_0(r)$ are not modified by the variations in density.

The random function $\epsilon(r)$ is created as follows. We first define a Fourier-filtered random function

$$\xi(r; \lambda) = \int dk \int dl \text{ rand } (l) e^{-k^2\lambda^2} e^{2\pi ik(r-l)}, \tag{21}$$

where $\xi(r;\lambda)$ varies with length scale larger than λ and rand (l) is a random function of l. We normalize $\xi(r;\lambda)$ as

$$\overline{\xi}(r;\lambda) = \frac{\xi(r;\lambda)}{\langle \xi(r;\lambda)\rangle_{\rm rms}}, \tag{22}$$

where $\langle X\rangle_{\rm rms}$ denotes the rms value of X. Therefore, the rms value of $\overline{\xi}$ is unity. We define the fractional density fluctuation $\epsilon(r) = \delta\rho/\rho$ as

$$\delta\rho/\rho = n(r)\overline{\xi}(r;\lambda_\rho), \tag{23}$$

where $n(r)$ represents an envelope of the fractional density fluctuation.

A uniform density fluctuation with rms amplitude of $n(r) = 0.1$ was used in van Ballegooijen & Asgari-Targhi (2016). In this paper, we applied nonuniform density variations based on observations described in Section 2 and presented in Figure 1. We carried out a series of nine simulations, three for each selected density fluctuation wavelength: $\lambda = 0.03$, 0.05, and $0.1\,R_\odot$. We created a time-independent, one-dimensional (1D) atmospheric model with density fluctuations and used it as the background atmosphere for the 3D RMHD simulation of the Alfvén waves. The boundary conditions and the method to solve the RMHD equations are identical to the smooth model described in Section 4.

Figure 4 shows the density fluctuation, the velocity amplitude of different types of waves, and the heating rates for the four curves shown in Figure 1(c) that approximate the observations. The wavelength of the density fluctuation is $\lambda = 0.03\,R_\odot$. Figure 4(a) shows the density fluctuation function $n(r)$ represented by the red curve. This curve is an estimated lower bound from the observations of Hahn et al. (2018) as discussed in Section 2. The envelope function is described by

$$n(r) = 0.12 - \left\{\frac{0.09}{[1 + 0.05(r-1) + 0.007(r-1)^3]^{6.96}}\right\}. \tag{24}$$

This function is plotted on the linear scale with both $+n(r)$ and $-n(r)$. The amplitude of the density fluctuations (black curve) are contained by the envelope function $n(r)$. Note that we had to artificially reduce the density fluctuations near the Alfvén critical point in order to allow the waves to cross over this point without increasing the wave reflection to the point where the computation would break down. The physical explanation is that without imposing this limit, the amplitude of the inward propagating waves Z_- becomes larger than the outward propagating waves Z_+ at the Alfvén critical point, resulting in a bottle-neck effect that could terminate the computation.

Figure 4(b) shows the simulation results for the rms velocity amplitude of the waves, the outward Z_+ waves, and the inward Z_- waves. We averaged these results over the cross section of the flux tube and over time. The $Z_-(r)$ waves show strong spatial variations and increase significantly compared to the smooth model shown in Figure 3(a). There are two dips in $Z_-(r)$ apparent at two positions, one is near $1.3\,R_\odot$ where the Alfvén speed has its maximum, which was also seen in the smooth model in Figure 3(a). The second dip is near the Alfvén critical point, approximately at $7\,R_\odot$. This is the point where we introduced a lower limit on the density fluctuations. The outward propagating waves $Z_+(r)$ shows very small spatial variations and remains largely unchanged.

Figure 4(c) shows the plasma heating rate $Q_{\rm A}(r)$ introduced in the setup of the background atmosphere, and the total heating rate $Q_{\rm tot}(r)$ arising from the simulated turbulence. The comparison between the heating rates in this model and the smooth model shown in Figure 3(d) demonstrates that as we introduce density fluctuations, the total heating rate $Q_{\rm tot}$ increases.

Figure 4(d) shows the density fluctuation envelope function describing the data set of Miyamoto et al. (2014). It smoothly connects the results across the slight gap in the observed height range and is defined by

$$n(r) = 10^{-3}\left[\frac{r^3}{1 + (r/5)^4}\right] + r^{-1}\left[1 - \frac{1}{1 + (r/5)^4}\right]. \tag{25}$$

Figure 4(e) shows the velocity amplitude of the outward Z_+ waves and inward Z_- waves. Figure 4(f) shows the wave energy dissipation rates per unit mass: the rate derived from the turbulence simulations, and the rate assumed in the setup of the background atmosphere.

Figure 4(g) applies the envelope function based on the observations of Hahn et al. (2018) and Miyamoto et al. (2014) combined. The density fluctuation is described by

$$n(r) = 0.217\exp-\left(\frac{r-7}{3.9}\right)^2 + 0.1452\exp - \left(\frac{r-1.345}{0.1}\right)^2 + \frac{10^{-3}r^3}{3.5 + (r/4.8)^3}. \tag{26}$$

Figure 4(j) shows the envelope function that is the upper bound to the observations of Hahn et al. (2018) and Miyamoto et al. (2014). It is described by

$$n(r) = 0.237 - \frac{0.217}{[1.0 + 3.86(r-1)^3]^{10}}. \tag{27}$$

The comparison between the four models in Figure 4 shows that the density fluctuation based on the combined observations, Figure 4(g), and the upper bound to the observations, Figure 4(j), create the largest inward propagating wave amplitudes. This in turn results in more interactions between inward and outward propagating waves and therefore creates stronger turbulence that increases the energy dissipation rate, as is shown in Figures 4(i) and (l) .

Figures 5 and 6 show the results of turbulence simulations for the cases of $\lambda = 0.05$ and $0.1\,R_\odot$, respectively. In each figure, the first column presents the density fluctuations and the envelope functions based on the observations and described by Equations (24)–(27). The second column shows the rms velocity amplitude of the waves, and the velocity amplitude of inward and outward propagating waves. The third column shows the heating rate assumed in the background atmosphere and the total heating rate from Alfvén wave turbulence due to the modeled density fluctuations.

In the last columns of Figures 4–6, the heating rate from turbulence mostly has a dip below $2\,R_\odot$. This may be due to Alfvén speed having a maximum near this height, as shown in Figure 2(d), which reduces the magnitude of the second term in Equation (6) and as a result, the amplitude of the inward propagating waves. The Elsässer variable of the inward waves Z_- has a dip at this height as is shown by the green curve in the second panels of Figures 4–6 and the heating rate that is the consequence of the interactions between inward and outward propagating waves is therefore reduced.

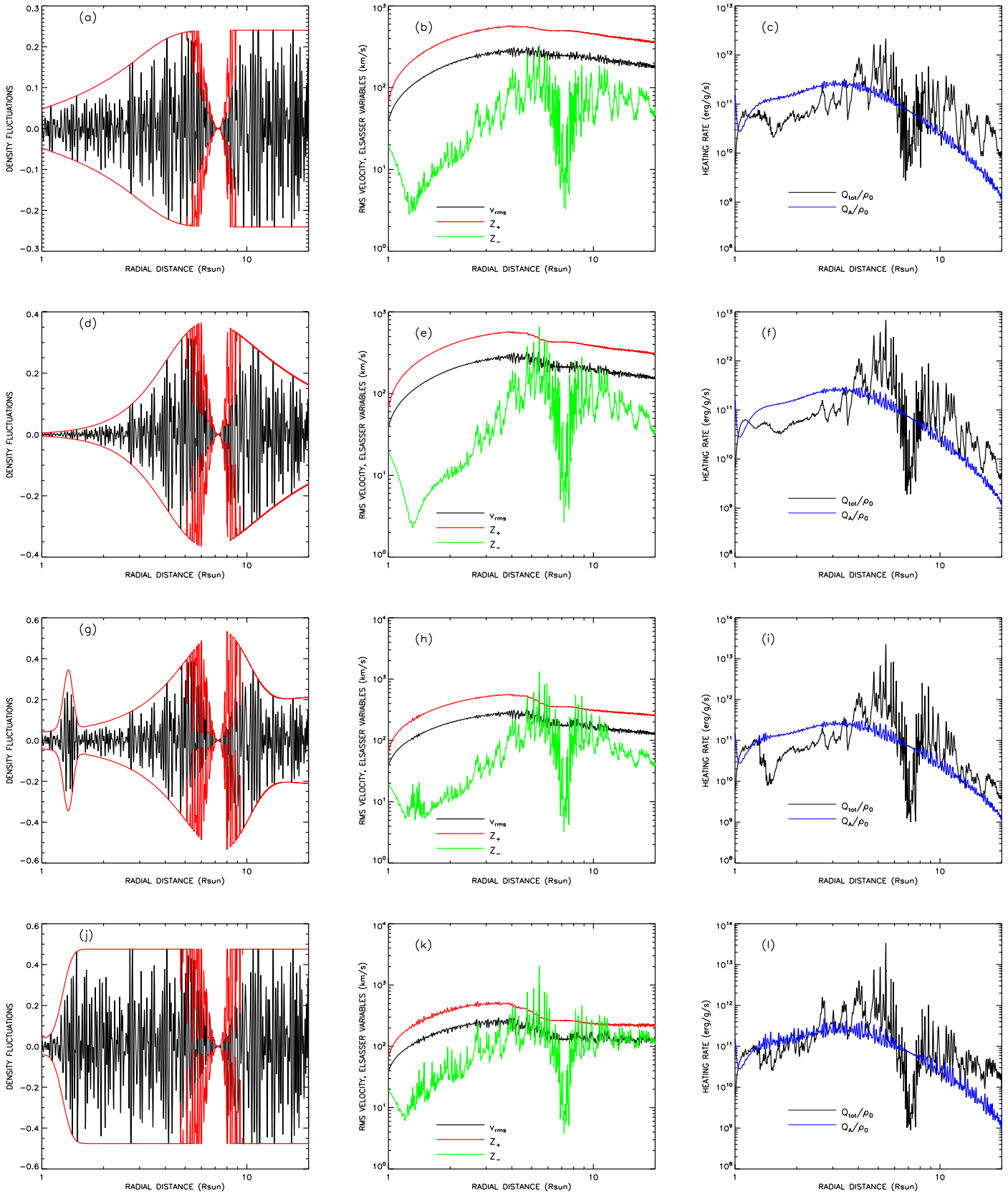

Figure 4. Radial dependence of model parameters for the case of $\lambda = 0.03\,R_\odot$. The first column, (a), (d), (g), and (j), shows the density fluctuation function $n(r)$ represented by the red curve based on observations by Hahn et al. (2018), Miyamoto et al. (2014), the two combined, and the upper bound to Hahn and Miyamoto's observations, respectively. The black curves show the randomly generated density fluctuations used for the simulations. The second column, (b), (e), (h) and (k), shows velocity amplitude of the waves (black curve), and the rms values of the Elsässer variables for outward Z_+ waves (red curve) and inward Z_- waves (green curve) for the different density fluctuation models. The third column, (c), (f), (i) and (l), shows the wave energy dissipation rates per unit mass from the different density fluctuation simulation (black curve), and that assumed in the setup of the background atmosphere (blue curve). Note that for each panel in each column, the y-axes minima and maxima can vary.

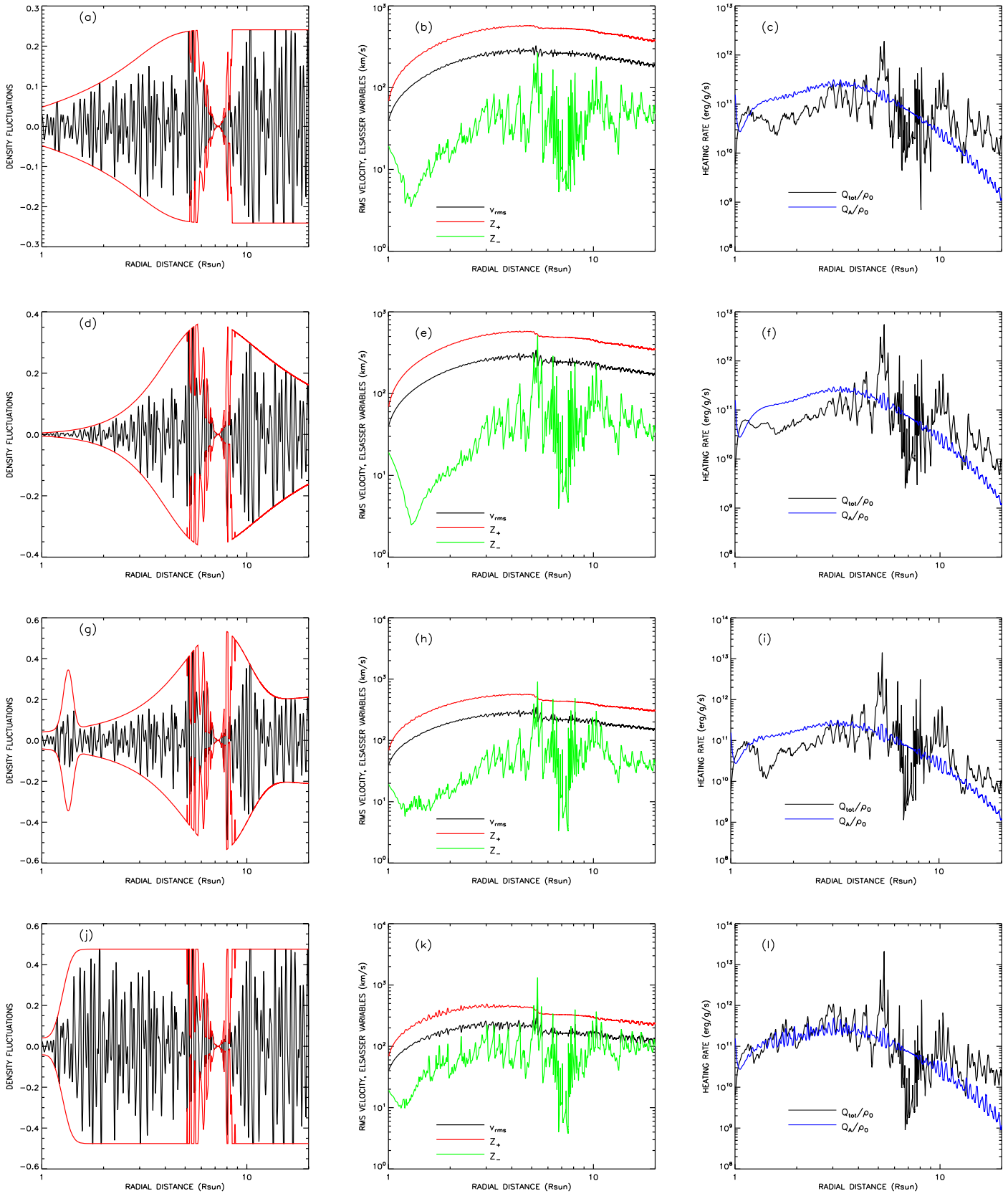

Figure 5. Same as Figure 4 but for $\lambda = 0.05\,R_\odot$.

6. Discussion and Conclusions

In this paper, we considered the effects of density fluctuations on the propagation, reflection, and dissipation of the Alfvén waves. These fluctuations have been attributed to compressive waves in solar wind (Kudoh & Shibata 1999; Moriyasu et al. 2004; Matsumoto & Shibata 2010). Here, we

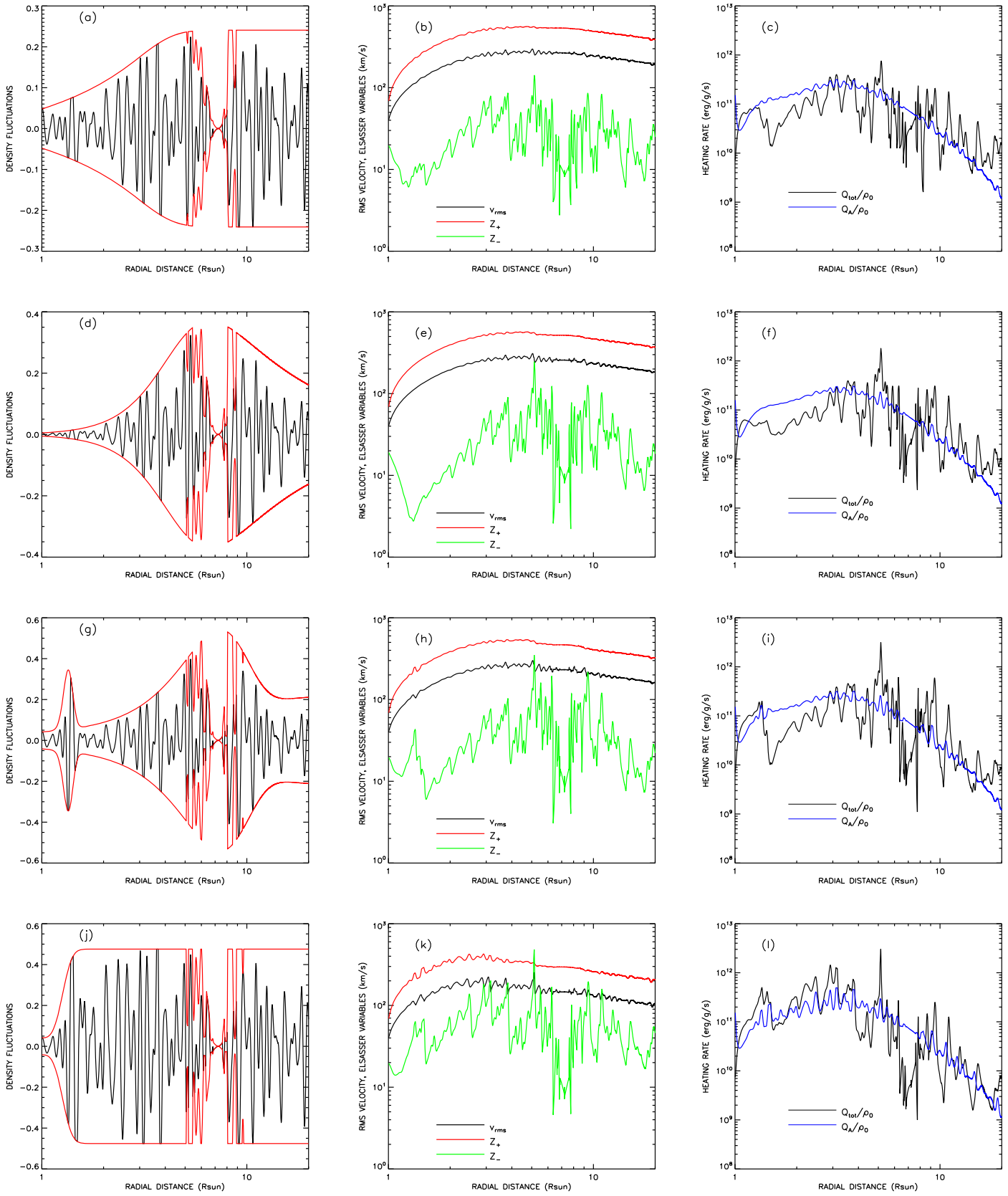

Figure 6. Same as Figure 4 but for $\lambda = 0.1\ R_\odot$.

considered nonuniform density fluctuations constrained by the observations of Hahn et al. (2018) and Miyamoto et al. (2014). We assumed the density fluctuations to have correlation lengths of the order of $\lambda = 0.03$, 0.05, and $0.1\ R_\odot$. These wavelengths are consistent with slow-mode compressive waves. The main results of the simulations presented in Figures 4–6 confirm that

the density fluctuations increase the wave reflection significantly, and as a result, enhance the amplitude of the inward propagating waves. The ratio of Z_-/Z_+ is about a factor of 10–15 larger than in the smooth model. This, in turn, increases the interactions between the inward and outward propagating waves and creates large wave dissipation rates. Therefore, the heating rate, which is the time-averaged dissipation rate, is increased significantly in all 12 models presented. All together, we find that density fluctuations on the order of $\sim$0.24 increase the turbulence to levels sufficient to heat the open field regions in coronal holes.

In our study, we simulated the Alfvén wave propagation from 1.003 to 20 $R_\odot$. Because, there are no single observations of density fluctuations from one instrument available within this height range, we combined observations from different instruments. For example, from 1 to 1.3 $R_\odot$, we used observation from SWAP instrument on board the Proba2 satellite (Hahn et al. 2018). For heights above 1.5 $R_\odot$, we used observations from Akatsuki spacecraft (Miyamoto et al. 2014). Combining observations from two instruments has certain disadvantages. Also, there is a gap between the heights of 1.3–1.5 $R_\odot$ where the SWAP instrument ended the observations, and the Akatsuki spacecraft began. Another problem with using multiple instruments is that they each have different resolution and systematic uncertainties that affect the reliability of the observations. We hope to carry out a similar study with the Parker Solar Probe when the spacecraft gets within the range of our Alfvén wave turbulence model.

We thank the referee for comments that helped to improve the paper. We are grateful to Dr. Takeshi Imamura from Japan Aerospace Exploration Agency for providing us with the data used in Miyamoto et al. (2014) from the Akatsuki mission. This project is supported under contract 80NSSC18K1207 from the NASA Heliophysics Supporting Research programto the Smithsonian Astrophysical Observatory (SAO) and Columbia University. SWAP is a project of the Centre Spatial de Liege and the Royal Observatory of Belgium funded by the Belgian Federal Science Policy Office (BELSPO).

Appendix
Constructing the Background Atmosphere in a Coronal Hole

The background atmosphere is a 1D time-independent model and is obtained by averaging the MHD equations over the cross section of the flux tube and over time. The detailed derivations of the equations are given in van Ballegooijen & Asgari-Targhi (2016, 2017). The parameters in the setup of the background atmosphere are introduced with the subscript 0. From the conservation of magnetic flux ϕ, we have

$$\phi = BA = \text{constant}, \tag{A1}$$

where B is the magnetic field and A is the flux tube cross section. Mass conservation along the flux tube from Equation (1) gives

$$\rho_0 u_0 / B_0 = \text{constant}, \tag{A2}$$

where ρ_0 is the plasma mass density and u_0 is the outflow velocity. The radial component of the equation of motion, Equation (2), is given as

$$\rho_0 u_0 \frac{du_0}{dr} = -\frac{dp_0}{dr} + D_{\rm wp} - \rho_0 \frac{GM_\odot}{r^2}. \tag{A3}$$

Here p_0 is the plasma pressure, and $D_{\rm wp}(r)$ is the wave pressure force. The wave-pressure force is computed from (Heinemann & Olbert 1980; Cranmer & van Ballegooijen 2005)

$$D_{\rm wp}(r) = -\frac{dU_{\rm mag}}{dr} + \frac{U_{\rm mag} - U_{\rm kin}}{H_{\rm B}}, \tag{A4}$$

where $U_{\rm mag}(r)$ and $U_{\rm kin}(r)$ are the time-averaged magnetic and kinetic energy of the waves, and $H_{\rm B}(r) \equiv B_0/(dB_0/dr)$ is the length scale for variations of the background field. To calculate $U_{\rm mag}$ and $U_{\rm kin}$, we need to solve the transport equations of the Elsässer variables (Cranmer & van Ballegooijen 2005; Verdini & Velli 2007; Verdini et al. 2010). We use the approximation

$$U_{\rm kin} \approx U_{\rm mag} \approx \frac{1}{2} U_{\rm A}, \tag{A5}$$

where $U_{\rm A}$ is the total energy density of the waves (see Appendices B and C in van Ballegooijen & Asgari-Targhi 2016 for a detailed derivation). Applying this, the transport equation of $U_{\rm A}$ is given by the wave-action conservation, which is an approximation for the wave energy equation

$$\frac{dS_{\rm A}}{dr} = -(1 + M_{\rm A}) \frac{Q_{\rm A}}{B_0}, \tag{A6}$$

where $S_{\rm A}(r)$ is the wave action per unit magnetic flux,

$$S_{\rm A}(r) \equiv \frac{(u_0 + v_{\rm A})^2 U_{\rm A}}{B_0 v_{\rm A}} = (1 + M_{\rm A})^2 \frac{U_{\rm A}}{\sqrt{4\pi\rho_0}}, \tag{A7}$$

and $M_{\rm A}(r) \equiv u_0/v_{\rm A}$ is the Alfvén Mach number. Here, we use $M_{\rm A} \propto \rho_0^{-1/2}$, which follows from Equation (A2) where $B_0 \approx v_{\rm A} \rho_0^{1/2}$, based on the definition of the Alfvén speed.

We write the energy Equation (3) as

$$Q_{\rm A} = Q_{\rm adv} + Q_{\rm rad} + Q_{\rm cond}, \tag{A8}$$

where $Q_{\rm A}(r)$ is the time-averaged heating rate, $Q_{\rm adv}(r)$ is the time average of the advection terms (the left-hand side of Equation (3)), and $Q_{\rm rad}(r)$ and $Q_{\rm cond}(r)$ are the energy loss rates due to radiation and thermal conduction, respectively. The right-hand side terms are calculated from

$$Q_{\rm adv}(r) = c_1 \rho_0 u_0 \left(\frac{1}{\gamma - 1} \frac{dT_0}{dr} - \frac{T_0}{\rho_0} \frac{d\rho_0}{dr} \right), \tag{A9}$$

$$Q_{\rm rad}(r) = n_{\rm e} n_{\rm H} \Lambda(T_0), \tag{A10}$$

$$Q_{\rm cond}(r) = B_0 \frac{d}{dr} \left(\frac{F_{\rm cond}}{B_0} \right), \tag{A11}$$

where $c_1 = 2.3 k_{\rm B}/(1.4 m_{\rm H})$ with $k_{\rm B}$ being the Boltzmann constant, $m_{\rm H}$ is the hydrogen mass, γ is the ratio of specific heat constants, $n_{\rm H}(r) = \rho_0/(1.4 m_{\rm H})$ is the hydrogen density, $n_{\rm e}(r) = 1.2 n_{\rm H}$ is the electron density, $\Lambda(T)$ is the radiative loss function (based on Figure 1 in Cranmer et al. 2007), and $F_{\rm cond}$ is the conductive flux. Since we only consider the coronal part of the flux tube, we neglect the effects of partial ionization on the internal energy of the plasma, and set $\gamma = 5/3$.

To compute $F_{\rm cond}$ we apply a "bridging law" for the parallel component of the thermal conductive flux,

$$F_{\rm cond}(r) = \frac{\nu_{\rm coll} F_{\rm SH} + \nu_{\rm exp} F_{\rm FS}}{\nu_{\rm coll} + \nu_{\rm exp}}, \tag{A12}$$

where

$$F_{\rm SH}(r) \equiv -\kappa dT_0/dr \tag{A13}$$

is the classical Spitzer–Harm prescription for thermal conduction, and

$$F_{\rm FS}(r) = 1.5\alpha_c n_{\rm e} u_0 k_{\rm B} T_0 \tag{A14}$$

is free-streaming heat flux that applies in the collisionless limit ($\alpha_c = 4$). Also, $\nu_{\rm coll}(r)$ is the electron–electron collision frequency; $\nu_{\rm exp} = u_0/|H_\rho|$ is the wind expansion rate, where $H_\rho(r) \equiv \rho_0/(d\rho_0/dr)$ is the density scale height; and κ is the conductivity. Note that the conductivity depends strongly on temperature, $\kappa \propto T_0^{5/2}$ (for details, see Cranmer et al. 2007).

The magnetic field $B_0(r)$ is assumed to be potential and is described by

$$B_0(r) = \sum_{n=1}^{5} B_n \left(\frac{r}{R_\odot}\right)^{-2n}, \tag{A15}$$

where $B_n = B_{\rm pole}[715,\ 2600,\ 2160,\ 832,\ 128]/6435$ with $n = 1, \cdots, 5$, and $B_{\rm pole}$ is the net flux density at the pole (we use $B_{\rm pole} = 10\,{\rm G}$). The temperature $T_0(r)$ is a known function of position (see van Ballegooijen & Asgari-Targhi 2016 for details) and is defined as

$$T_0(r) = T_c \frac{C_0}{B_0(r)} \sum_{n=1}^{5} B_n \left(\frac{r}{R_\odot}\right)^{-2n} f_n(r), \tag{A16}$$

where

$$T_c = \frac{GM_\odot}{c_1 R_\odot}, \tag{A17}$$

$$f_n(r) = \left[\frac{1}{2n+m}\left(\frac{r}{R_\odot}\right)^{-m} - \frac{C_1}{2n+m+k}\left(\frac{r}{R_\odot}\right)^{-m-k}\right], \tag{A18}$$

with C_0 and C_1 as dimensionless constants. For the temperature to decrease with r at large height, we require $m > 0$. To construct the background atmosphere, we solve the equations presented in this section iteratively. The equations are solved numerically where the lower boundary of the model is at $r = 1.003\ R_\odot$ and the upper boundary is at $r = 20\ R_\odot$ (see van Ballegooijen & Asgari-Targhi 2016, 2017 for details).

ORCID iDs

M. Asgari-Targhi https://orcid.org/0000-0003-0204-8385
M. Hahn https://orcid.org/0000-0001-7748-4179
D. W. Savin https://orcid.org/0000-0002-1111-6610

References

Alfvén, H. 1947, MNRAS, 107, 211
Banerjee, D., Gupta, G. R., & Teriaca, L. 2011, SSRv, 158, 267
Banerjee, D., Pérez-Suárez, D., & Doyle, J. G. 2009, A&A, 501, L15
Belcher, J. W. 1971, ApJ, 168, 509
Bemporad, A., & Abbo, L. 2012, ApJ, 751, 110
Chandran, B. D. G., Quataert, E., Howes, G. G., Hollweg, J. V., & Dorland, W. 2009, ApJ, 701, 652
Cranmer, S. R., Asgari-Targhi, M., Miralles, M. P., et al. 2015, RSPTA, 373, 20140148
Cranmer, S. R., & van Ballegooijen, A. A. 2005, ApJS, 156, 265
Cranmer, S. R., van Ballegooijen, A. A., & Edgar, R. J. 2007, ApJS, 171, 520
De Pontieu, B., McIntosh, S. W., Carlsson, M., et al. 2007, Sci, 318, 1574
Dmitruk, P., Matthaeus, W. H., Milano, L. J., et al. 2002, ApJ, 575, 571
Grappin, R., Frisch, U., Léorat, J., & Pouquet, A. 1982, A&A, 105, 6
Grappin, R., Pouquet, A., & Léorat, J. 1983, A&A, 126, 51
Hahn, M., D'Huys, E., & Savin, D. W. 2018, ApJ, 860, 34
Hahn, M., Landi, E., & Savin, D. W. 2012, ApJ, 753, 36
Hahn, M., & Savin, D. W. 2013, ApJ, 763, 106
Halain, J.-P., Berghmans, D., Seaton, D. B., et al. 2013, SoPh, 286, 67
Hara, H. 2019, ApJ, 887, 122
Heinemann, M., & Olbert, S. 1980, JGR, 85, 1311
Hollweg, J. V. 1973, ApJ, 181, 547
Hollweg, J. V., & Isenberg, P. A. 2007, JGR, 112, 8102
Jacques, S. A. 1978, ApJ, 226, 632
Krieger, A. S., Timothy, A. F., & Roelof, E. C. 1973, SoPh, 29, 505
Kudoh, T., & Shibata, K. 1999, ApJ, 514, 493
Landi, E., & Cranmer, S. R. 2009, ApJ, 691, 794
Matsumoto, T., & Shibata, K. 2010, ApJ, 710, 1857
Matthaeus, W. H., Zank, G. P., Oughton, S., Mullan, D. J., & Dmitruk, P. 1999, ApJL, 523, L93
McIntosh, S. W., De Pontieu, B., & Tarbell, T. D. 2008, ApJL, 673, L219
Miyamoto, M., Imamura, T., Tokumaru, M., et al. 2014, ApJ, 797, 51
Moriyasu, S., Kudoh, T., Yokoyama, T., & Shibata, K. 2004, ApJL, 601, L107
Morton, R. J., Tomczyk, S., & Pinto, R. 2015, NatCo, 6, 7813
Munro, R. H., & Withbroe, G. L. 1972, ApJ, 176, 511
Parker, E. N. 1965, SSRv, 4, 666
Perez, J. C., & Chandran, B. D. G. 2013, ApJ, 776, 124
Santandrea, S., Gantois, K., Strauch, K., et al. 2013, SoPh, 286, 5
Seaton, D. B., Berghmans, D., Nicula, B., et al. 2013, SoPh, 286, 43
Singh, J., Hasan, S. S., Gupta, G. R., Nagaraju, K., & Banerjee, D. 2011, SoPh, 270, 213
Suzuki, T. K., & Inutsuka, S. I. 2006, JGRA, 111, A06101
Tian, H., DeLuca, E. E., Cranmer, S. R., et al. 2014, Sci, 346, 1255711
Tomczyk, S., & McIntosh, S. W. 2009, ApJ, 697, 1384
Tomczyk, S., McIntosh, S. W., Keil, S. L., et al. 2007, Sci, 317, 1192
van Ballegooijen, A. A., & Asgari-Targhi, M. 2016, ApJ, 821, 106
van Ballegooijen, A. A., & Asgari-Targhi, M. 2017, ApJ, 835, 10
van Ballegooijen, A. A., Asgari-Targhi, M., Cranmer, S. R., & DeLuca, E. E. 2011, ApJ, 736, 3
Velli, M. 1993, A&A, 270, 304
Velli, M., Grappin, R., & Mangeney, A. 1989, PhRvL, 63, 1807
Verdini, A., & Velli, M. 2007, ApJ, 662, 669
Verdini, A., Velli, M., & Buchlin, E. 2009, ApJL, 700, L39
Verdini, A., Velli, M., Matthaeus, W. H., Oughton, S., & Dmitruk, P. 2010, ApJL, 708, L116
Wilhelm, K., Marsch, E., Dwivedi, B. N., et al. 1998, ApJ, 500, 1023
Zhou, Y., & Matthaeus, W. H. 1990, JGR, 95, 10291
Zirker, J. B. 1977, Coronal Holes and High Speed Wind Streams (Boulder, CO: Colorado Assoc. Univ. Press)